Feature Article

X-Ray Absorption Spectroscopy: A Complementary Tool for Structural and Electronic Characterization of Solids

Jean Etourneau

Institut de Chimie de la Matière Condensée de Bordeaux (ICMCB)-CNRS
87, avenue du Dr A. Schweitzer-33608 Pessac Cedex, France
Received October 21, 1997

The purpose of this paper is to show that X-ray absorption spectroscopy (XANES and EXAFS) is a powerful technique for characterizing both crystalline and amorphous solids from structural (local order) and electronic point of view. The principle of this technique is briefly described by showing the main factors which must be considered for recording and fitting the experimental results. Some non-trivial examples have been selected for demonstrating that XAS spectroscopy is the only technique for bringing a definitive answer as for example: the determination of the local distortion of the NiO_6 octahedra in the $Li_{1-z}Ni_{1+z}O_2$ layered oxides and the evidence of the presence of copper pairs in the NASICON-type phosphate $CuZr_2(PO_4)_3$. Are also reported some significant examples for which XAS spectroscopy is decisive with other characterization methods as (i) Raman spectroscopy for glasses (ii) Mössbauer spectroscopy for $LiNi_{1+z-t}Fe_tO_2$ oxides (iii) magnetic measurements for Ce-based intermetallic compounds.

Introduction

The understanding of the macroscopic properties of solids requires the knowledge of such systems at the microscopic scale. The methods that are used depend on whether the substance is molecular or non-molecular. However whatever the substance it is necessary to determine the relative positions of the atoms in the considered system and to know for example the ground states properties and possible excitation of the valence electrons and conduction electrons if any.

For molecular materials, details of the molecular geometry may be obtained from further spectroscopic measurements and in the case where the molecules pack together in a crystalline state, X-ray diffraction technique can be used for structure determination.

For non molecular solids, it is necessary to clarify the two following main points:
- the form of the solid (single crystal or polycrystalline powder)
- the crystal structure (local and long range ordering)

and the crystal defects.

No single techniques is able to provide a complete characterization of a solid and a variety of techniques is used in combination involving diffraction, microscopic and spectroscopic techniques.

Although many of the spectroscopic techniques were initially developed for and applied to molecular materials, often liquids and gases, they are finding many applications in solid state chemistry for example. Spectroscopic measurements on solids are complementary to X-ray or electron diffraction studies for instance, since spectroscopy gives information on local order whereas diffraction deals mainly with long range order.

There are many different spectroscopic techniques but all involve the same basic principle in which materials absorb or emit energy. This energy is usually electromagnetic radiation as in the case of (i) vibrational spectroscopy (IR and Raman) (ii) visible and ultra-violet spectroscopy (iii) nuclear magnetic resonance (NMR) (iv) electron spin resonance (ESR) (v) Mössbauer spectroscopy (vi) spectroscopies

as: X-ray and UV photoelectron spectroscopies (XPS, UPS); Auger electron spectroscopy (AES); electron energy loss spectroscopy (EELS) (vii) X-ray absorption spectroscopies.

In the present paper there are the spectroscopies involving X-ray absorption which will draw our attention since both electronic properties and local atomic order are relevant to this type of technique.

After giving briefly the general principle of the X-ray absorption spectroscopy, significant examples will be chosen in the field of solid state chemistry and molecular chemistry, for showing that X-ray absorption spectroscopy (XAS) is complementary to other techniques or in some cases it is the only method for bringing structural information.

Principle and Interest of the X-Ray Absorption Spectroscopy (XAS)[1-4]

The X-ray absorption spectroscopy is based upon the absorption of X-rays by samples, especially at energies in the region of absorption edges corresponding to the ionization of *K, L, etc.* shells of the atoms embedded in condensed matter. They are powerful techniques for studying local crystal structure and probing electronic structure of the solids but are easily accessible only with a synchrotron radiation source.

The absorption of the matter by X-rays follows the classical Beer-Lambert law

$$\mu x = \log(I_0/I)$$

where I is the intensity of transmitted beam for an incident intensity I_0, x is the thickness of the sample and μ is the linear absorption coefficient of the material.

X-ray absorption spectra can be divided into two regions which contain roughly complementary information, XANES and EXAFS as shown in Figure 1.

The X-ray absorption near edge structure (XANES).

XANES region corresponds to an absorption edge in which fine structure is associated with inner shell transition. The origin of XANES is relatively complex and depends on a number of effects which are not completely characterized so far. However XANES can provide a unique information about oxidation state of the probing atom, site symmetry and the nature of the bonding with surrounding ligands in a broad range of materials.

The extended X-ray absorption fine structure (EXAFS).

Whereas the XANES regime deals with the details of the fine structure in the region of an absorption edge, the EXAFS technique[2] is relative to the variation of absorption with energy over a much wider range, extending out from the absorption edge to higher energies.

In the EXAFS region, spectra appears a ripple of the X-ray absorption whose origin lies in the back-scattering of the photoelectron. The modulation of the absorption is caused by interference between the outgoing wave emitted by the absorber atom and the backscattered wave coming from the surrounding atoms. Depending on the optical path, the interference can be constructive or destructive. Since the interference depends on the phase of the back-scattered wave functions, the effect is sensitive to the phase-shift associated with the backscattering and therefore to the distances to the neighbouring atoms. From the periodic modulation of the
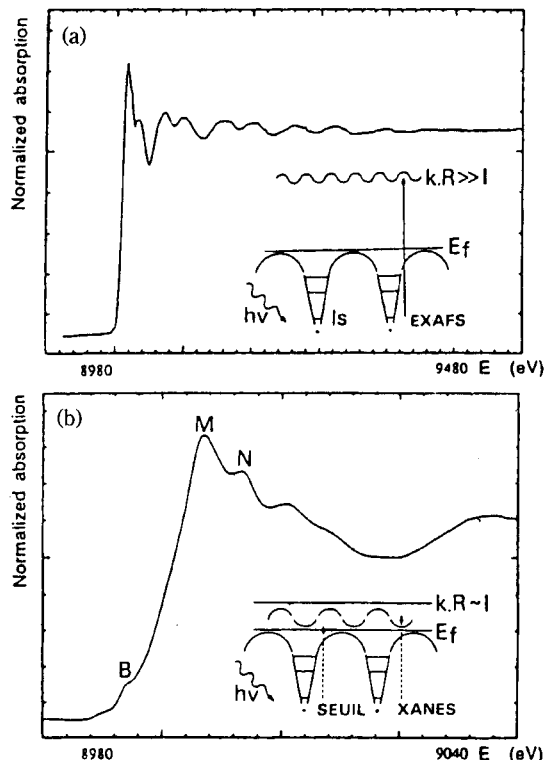
Figure 1. Definition of EXAFS (a) and XANES (b) regions leg. Cu K-edge spectrum).

absorption plotted against the electron momentum, we can deduce precisely by using Fourier transform techniques, the distance between the absorbing central atom and the neighbouring ones.[5] The Fourier transform of the modulation of the X-ray absorption spectra looks like a radial distribution function (RDF). Furthermore the intensity of the modulation contains information about the coordination number, but its determination is clearly less reliable.

The EXAFS formalism for condensed matter is based on the Fermi's gold rule which gives the probability of transition for a photoelectron between an initial state $|i>$ and a final state $|f>$, both of which are multi-electronic wave functions. In other words this probability corresponds to the X-ray absorption which is given in quantum mechanics by the following expression:

$$\mu \approx \sum_i^f |<i \mid H_{int} \mid f>|^2 \delta(E_f - h\omega)$$

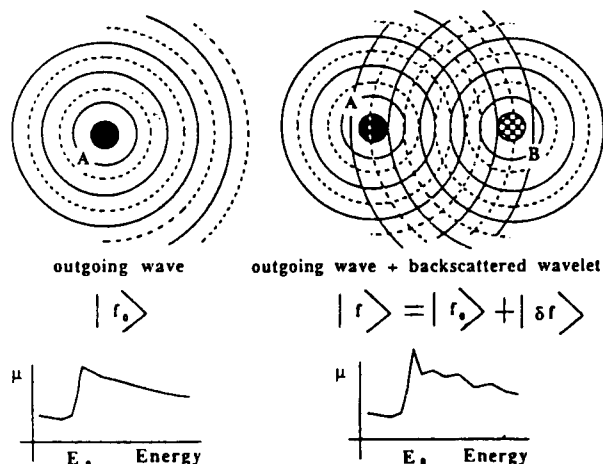$- H_{int}$ is the interaction Hamiltonian in the dipolar approximation

$-$ the δ function expresses energy conservation where is the energy of the photon and $(E_f - E_i)$ is the energy difference between the initial state $|i>$ and the final state $|f>$.

Let us note that for an isolated atom A the final state of the one electron transition is just an outgoing wave $|f_o>$ whereas in a AB diatomic system the final state $|f>$ consists of two terms: (i) the atomic term $|f_o>$ (ii) a back-scattering term $|d_f>$ (Figure 2).

Thus the final state can be written as follows

$$|f> = |f_o> + |d_f> = |\,|f_o>(l + \chi_{(E)})$$

$\chi_{(E)}$ represents the EXAFS modulation which can be deduc-

X-Ray Absorption Spectroscopy

Bull. Korean Chem. Soc. **1998**, Vol. 19, No. 1   7

Figure 2. For an isolated atom the final state of the one electron transition is just an outgoing wave. The EXAFS spectrum of a diatomic molecule is caused by interference between the outgoing wave and the backscattered wave. According to the optical path (2k.r), the interference can be constructive or destructive.

ed from the X-ray absorption cross section:

$$\chi_{(E)} = \chi_{(k)} = \frac{\mu(E) - \mu_1(E)}{\mu_1(E) - \mu_0(E)}$$

- k is the photoelectron wave-vector, evaluated using $\hbar^2 k^2 = 2m(E - E_0)$
- E is the energy of the X-ray photon
- E_0 is a reference energy
- m is the mass of the electron
- $\mu(E)$ is the energy dependent oscillations of the absorption cross-section
- $\mu_1(E)$ is the atomic absorption
- $\mu_0(E)$ is the extrapolation of the pre-edge absorption

The extraction of the EXAFS signal from X-ray absorption spectrum is schematicaily represented on Figure 3.

By including the relevant phase-shifts and in the framework of the plane wave approximation $\chi(k)$ can be written as

$$\chi_{(k)} = \sum_j A_j(k)\ \sin(2kR_j + \varphi_j)$$

The summation is over J coordination shells, R_j is the distance from the absorber to the jth shell and φ_j is the total
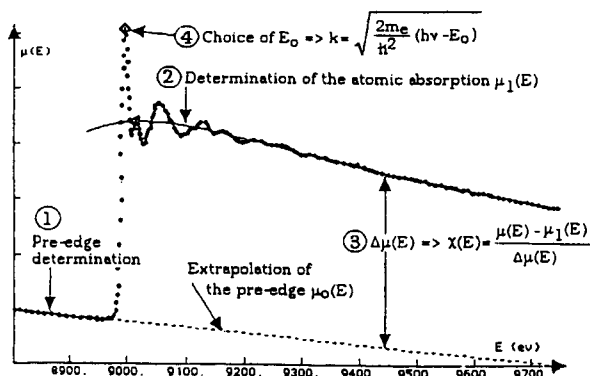
Figure 3. Extraction of the EXAFS signal from the X-ray absorption spectrum.

phase shift.

$A_j(k)$ which represents the total jth shell scattering amplitude and can be expressed as

$$A_j(k) = \frac{N_j}{kR_j^2}\ F_j(k)\ \exp-(2\sigma_j^2 k^2)$$

N_j and σ_j represent the number of atoms in the jth shell and the root-mean square deviation of the interatomic distances over R_j which results both from static and from thermal disordering effects, respectively.

$$F_j(k) = f_j(\pi, k)\exp\left(-\frac{2R_j}{\lambda}\right)$$

where $f_j(\pi, k)$ is the back-scattering amplitude which looks like an electron-back-scattering form factor and λ is the mean free path of the photoelectron.

The argument of the total scattering amplitude $A_j(k)$ is $(2kR_j + \varphi_j)$ where

$2kR_j$ is the optical path (~80% contribution)

$\varphi_j = 2\delta_A + \theta_j$

- δ_A is the phase change (~15% contribution) that the photoelectron undergoes in the deep part of the potential of the central atom A on each trip forth and back

- θ_j is the argument of the $f(\pi, k)$ backscattering amplitude (~5% contribution).

From practical point of view the experimental EXAFS spectra $\chi(k)$ are often analyzed by using standard methods in the plane wave approximation. This approximation can be justified by using model compounds with similar bond lengths and therefore phase-shifts and amplitudes. After the substraction of the background and of the atomic absorption $\mu_1(E)$ the EXAFS contribution to the various coordination shells around the absorber are isolated by applying a k^2 or k^3 weighted Fourier transform of $\chi(k)$ from k space to R space in order to magnify the weak EXAFS signal at large k. The resulting peaks of the radial structure function (RDS) which correspond to individual coordination shells are back-Fourier transformed, leading to filtered EXAFS functions which are finally fitted to the parameterized following expression:

$$\chi(k) = \sum_j A_j(k)\ \sin(2kR_j + \varphi_j)$$

$$A_j(k) = \underbrace{\left[s_0^2 \frac{1}{kR_j^2}\exp\left(-\frac{2R_j}{\lambda(k)}\right)\right]}_{damping} \underbrace{\left[N_j f_j(pi, k)\right]}_{scattering} \underbrace{\left[\exp(-2\sigma_j^2 k^2)\right]}_{disorder}$$

, where s_0^2 is a scale factor (relaxation, multi-electron excitations)

In the total scattering amplitude $A_j(k)$ appears three main contributions showing the damping, scattering and disorder effects.

The least square fit of the filtered EXAFS functions involves adjustable parameters: R_j (± 0.02 Å from the absorber), N_j (the coordination number is known generally with poor accuracy), σ^2 (closely related to N_j) and the edge position E_0 which appears in expression giving the k wave vector (see above).

The number of parameters used for the fit of the filtered

EXAFS function can be determined by the empirical expression:[6]

$$n_{(parameters)} = \frac{2\Delta k\,\Delta R}{\pi}$$

, where ΔR is the width of the filtering window
Δk is the width of the simulated spectrum.

In other words two bond lengths differing by ΔR can only be separated if $\Delta k\Delta R > \pi/2$.

Although the phase-shifts δ_A and θ_j and the backscattering amplitudes $f_j(\pi, k)$ are theoretically known for practically all the atoms,[7] nevertheless the best way is to measure them in a model compound, the structure of which is well known and chemically close to that of the unknown sample under investigation.

In conclusion EXAFS is a powerful technique, equally suitable for non-crystalline as well as crystalline materials, for determining the local structure as bond distances and with a certain caution the coordination number. Thus, it is particularly interesting to study disordered and amorphous materials such as glasses, gels and amorphous metals since their structural information is generally hard to obtain. This technique is also useful for studying solid surfaces (SEXAFS).[3]

Let us point out that EXAFS has one great advantage: by tuning in to the absorption edge of each element present in the material, a partial RDF for each element may be established. By contrast conventional X-ray diffraction techniques give only a single averaged RDF for all the elements present.

Before illustrating the interest of XAS in solid state chemistry by some relevant examples, it is worthwhile noting some points concerning the XANES and EXAFS regimes.

In the EXAFS regime, the modulation of the X-ray absorption cross section is dominated by simple backscattering paths from nearby atoms. For XANES regime, the mean free path of the photoelectron can be much larger and the probability of off-linear scattering increases. Both of these differences tend to increase the number of scattering paths which contribute significantly to the X-ray absorption cross section. In particular higher order scattering, *i.e.* multilegged paths involving several atoms, it become more important. Essential features of successful scattering formulation for XANES include the consideration of multiple scattering paths and due to this fact the interpretation of XANES is complicated as well as the non validity of the plane-wave-scattering approximation applicable in the EXAFS range. However the relevant methods for a numerical interpretation of the XANES range of bulk solids are, on one hand electronic density of state (DOS) calculations, and, on the other hand, single and multiple-scattering (MS) calculations.[8]

It is also well established that (MS) may contribute significantly to EXAFS in a way that new peaks can be induced in the radial distribution function (RDF) around the absorbing atom, which is obtained by Fourier transformation of the EXAFS spectrum. Very clear examples have been recently shown in perovskite compounds such as tungsten and rhenium oxides[9,10] and expanded to various structures based on MO_4 and MO_6 clusters.[11]

For knowing the importance of the multiple scattering contribution, a great care must be taken in the choice of both

the energy range of the EXAFS analysis and the weighting window in the Fourier transform. This remark is well illustrated in the study of the iridium oxide.[12] Let us note that the multiple-scattering analyses of the EXAFS data are generally performed by using the FEFF code.[13,14]

Xas Used for Solving Non-Trivial Problems in the Characterization of Solids

Some significant chemical systems are presented here for demonstrating that XAS spectroscopy (XANES and EXAFS) is complementary to other techniques for characterizing crystalline or non-crystalline solids from structural and electronic point of view, at the local level: formation of clusters, location of dopants in crystal structures, site distortion and local structure of glasses determined by EXAFS, site symmetry, oxidation state and intermediate valence state studied by XANES. We have focused on systems that have (i) important technological applications: namely $Li_{1-z}Ni_{1+z}O_2$ and $LiNbO_3$ (ii) outstanding optical properties in $CuZr_2(PO_4)_3$, silicate and borophosphates glass matrices containing TiO_2 and tellurite glasses (iii) peculiar magnetic and electrical behaviors resulting from valence fluctuations in Ce-based intermetallic compounds.

### Characterization of local structures in crystalline solids.

The layered oxide $Li_{1-z}Ni_{1+z}O_2$. The electrochemistry and the structural chemistry of layered nickel oxide A_xNiO_2 (A=Li, Na) have been extensively studied as a result of its technological importance as positive electrode material in rechargeable lithium ion batteries (particularly rocking-chair ones using a carbon negative electrode).[15-18]

In order to understand the electrochemical behavior of the lithium nickel oxides it is necessary to know precisely the evolution of their structure and the mechanism leading to the nickel oxidation during the electrochemical cycling, in other words at the time of the lithium intercalation-(discharge)-deintercalation (charge).

Lithium nickelates exhibit a layered structure made of NiO_2 slabs built up of edge-sharing NiO_6 octahedra: the monovalent lithium cations are inserted between these slabs in octahedral coordination (Figure 4). Previous crystallographic studies have clearly shown that the true formula of lithium nickelates is $Li_{1-z}Ni_{1+z}O_2$ ($0.05 \le z \le 0.20$) instead of $LiNiO_2$.[19,20] There are $2z$ nickel in the divalent state and z extra nickel ions are located in the interslab space. Thus the formula representing the Ni charge distribution is:[21]

$$(Li_{1-z}Ni_z^{II})_{interslab}(Ni_z^{II}Ni_{1-z})_{intraslab}O_2$$
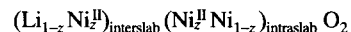
Since the electrochemical study of these nickelates involves the lithium intercalation-deintercalation mechanism, their formula hereafter will be depicted as $Li_{x-z}Ni_{1+z}O_2$. For $0.75 \le x \le 1$ the structure exhibits a rhombohedral symmetry, and for $0.5 \le x \le 0.75$ the symmetry is monoclinic.[22] The main features of the electrochemical studies performed up to now can be roughly summarized as follows (i) a systematic study of the open circuit voltage (OCV) cycling curve (Figure 5) shows that the irreversible domain x depends strongly on the z extra nickel content (ii) the nickel ion distribution is never modified by cycling in the 3.0-4.1 V (iii) the best performances for a positive electrode are ob-
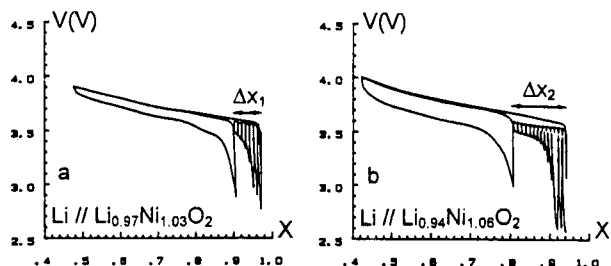
X-Ray Absorption Spectroscopy

Bull. Korean Chem. Soc. **1998**, Vol. 19, No. 1   9
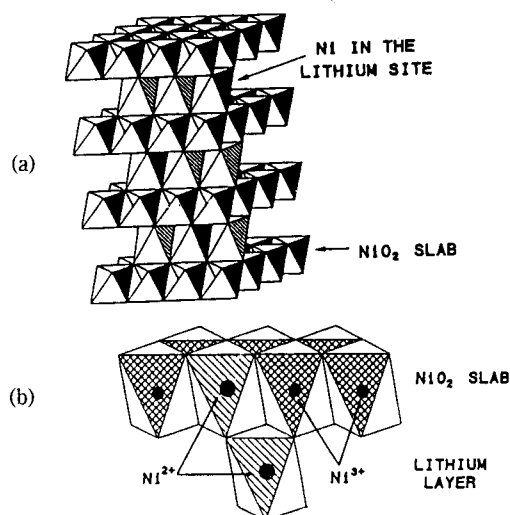
Figure 4. (a) Perspective view of the $Li_{1-z}Ni_{1+z}O_2$ structure. (b) Partial view of the $Li_{1-z}Ni_{1+z}O_2$ structure showing the existence of divalent nickel ions in the slab and in the interslab space.

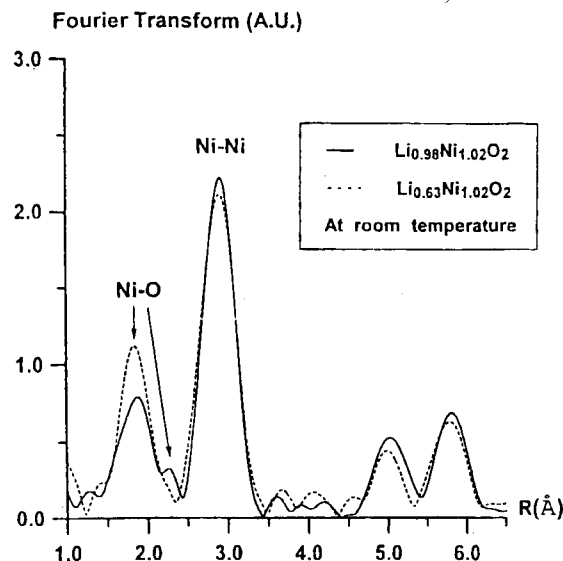**Figure 6.** Experimental Fourier transforms for Ni K-edge EXAFS of $Li_{0.98}Ni_{1.02}O_2$ and $Li_{0.63}Ni_{1.02}O_2$ phases.

tained for $z \leq 0.03$.[23]

The X-ray diffraction studies were not enough relevant for explaining the structural behavior of the lithium nickelates and two main questions were raised (i) why a macroscopic structural distortion is not observed for $Li_{0.98}Ni_{1.02}$-O_2 (the better composition obtained with respect to the ideal stoichiometric compound $LiNiO_2$) while it is seen for the isostructural compound $NaNiO_2$. (in both compounds, Ni^{3+} which is in a low spin state $t_{2g}^6 e_g^1$ as shown by magnetic measurements, induces a strong Jahn-Teller effect), (ii) how we can explain the nature of the monoclinic distortion which occurs in the wide $0.5 \leq x \leq 0.75$ composition range.

For trying to answer the two questions, EXAFS experiments have been performed on two compounds: $Li_{0.98}Ni_{1.02}$-O_2 and $Li_{0.63}Ni_{1.02}O_2$ EXAFS spectra were collected on the station of the SERC (Daresbury Synchrotron Radiation Source in UK) for $Li_{0.98}Ni_{1.02}O_2$[24,25] and on the station EXAFS III at LURE-ORSAY in France for $Li_{0.63}Ni_{1.02}O_2$.[26,27] In both cases Ni-K edge data were collected in transmission mode both at room temperature and at liquid nitrogen temperature, using a Si(1 1 1) monochromator. The storage ring was operating with a 150-250 mA beam current. The EXAFS oscillations were analyzed with the Daresbury suite of EXAFS programs (EXCALIB, EXBACK and EXCURV 92). More details are given in ref. 24-27. However let us mention that (i) pure NiO was employed as a model com-

Figure 5. Correlation between the reversible composition range and the loss of reversibility at the first cycle for two oxides: $Li_{0.97}Ni_{1.03}O_2$ and $Li_{0.94}Ni_{1.06}O_2$.

pound to determine non-structrual parameters such as the phase shifts and the back scattering factors (ii) the multiple scattering contribution has been removed since in the lithium nickelate structure the multiple scattering paths with O-Ni-O angle, at centered absorbing atom equal to 90°, vanishes in the case fo K-edge, Thus the multiple scattering effects do not affect the first Ni-O and the second Ni-Ni shells. Therefore, in order to refine both shells up to 3 Å, it was enough to use only the single scattering contribution.

For both compounds the Fourier transforms which have been obtained by Fourier filtering procedure between 1.4 Å $<R<6$ Å of the Ni K-edge EXAFS spectra are shown in Figure 6. The spectra contain information on many coordination shells. In fact five main peaks on the Fourier transform are distinguishable up to a radial distance of 6 Å.

$Li_{0.98}Ni_{1.02}O_2$.[24,25] Since the X-ray diffraction data do not show structural distortion, only an EXAFS study was able to identify any Local distortion of the structure. Therefore the attention was focused on the first two coordination shells which were isolated in the raw data by Fourier filtering procedures.

The first shell (14 Å $<R<2.4$ Å) corresponds to only Ni-O interactions (NiO_6 octahedra). For this shell only five independent parameters [the radial distance (R), the edge position (E_0) and the Debye Waller factors ($2\sigma^2$)] were refined. Due to the strong correlation between σ^2 and the coordination number N, this later was assumed to be 6.

Two models were proposed for the fitting of the first shell: (i) the first one was carried out with only one Ni-O bond length of 1 97 Å (deduced from Rietveld analysis) (ii) the second one takes into account two different Ni-O distances (four short distances and two long ones as for $NaNiO_2$). The best fit is obtained with the second model as shown in the Fourier transform (Figure 7). The data are summarized in Table 1.

In the second shell, two types of interactions are distinguished (Ni-Ni and Li-Ni). Due to the fact that the back-scattering amplitude is weak for Li with respect to that of Ni, the contribution of the Li shell to the EXAFS spectra
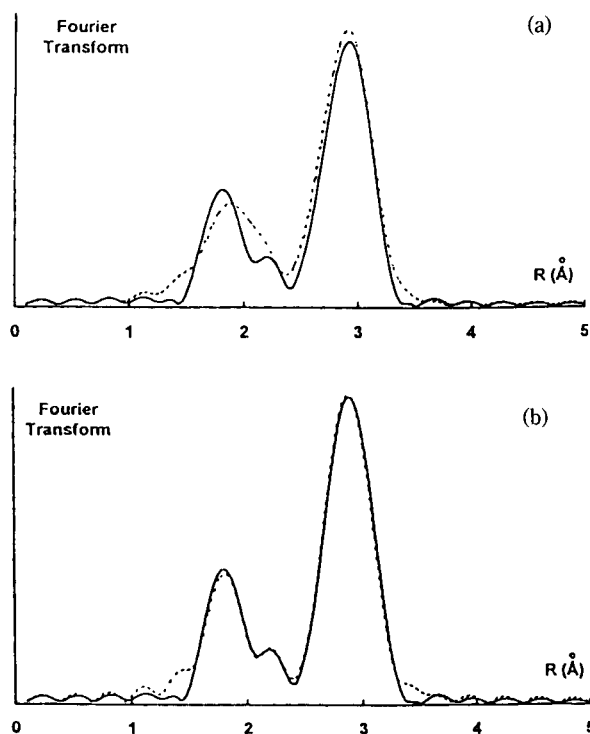
Figure 7. Comparison between the Fourier transforms of EX-AFS spectra of $Li_{0.98}Ni_{1.02}O_2$. Solid line is experiment and dashed line is the model fit (a) N_1=6; R_1=1.97 Å and N_2=6; R_2=2.87 Å (b) N_1=4; R_1=1.91 Å and N_1=2; R_1=2.09 Å and N_2=6; R_2=2.87 Å.

Figure 8. (a) Comparison between the EXAFS spectrum of $Li_{0.98}Ni_{1.02}O_2$ and model fits. The solid line is the Fourier filtered k^3 weighted absorption χ. The dashed line is the model fit. (b) Comparison between the Fourier transform of the results reported in Fig. 8a. Solid line is experiment and dashed line is the model fit. N_1=4; R_1=1.91 Å and N_1=2; R_1=2.09 Å and N_2=2; R_2=2.79 Å and N_2=4; R_2=292 Å

has been neglected. From the results obtained with the first shell, showing a local distortion of the NiO_6 octahedra, two different Ni-Ni distances were expected in the second shell. As shown in Figure 8 this hypothesis leads to a large discrepancy between the experimental curves (EXAFS oscillations and Fourier transform) and the simulated ones. The experimental results show that the best fit is obtained with only one Ni-Ni distance (Table 2 and Figure 7).
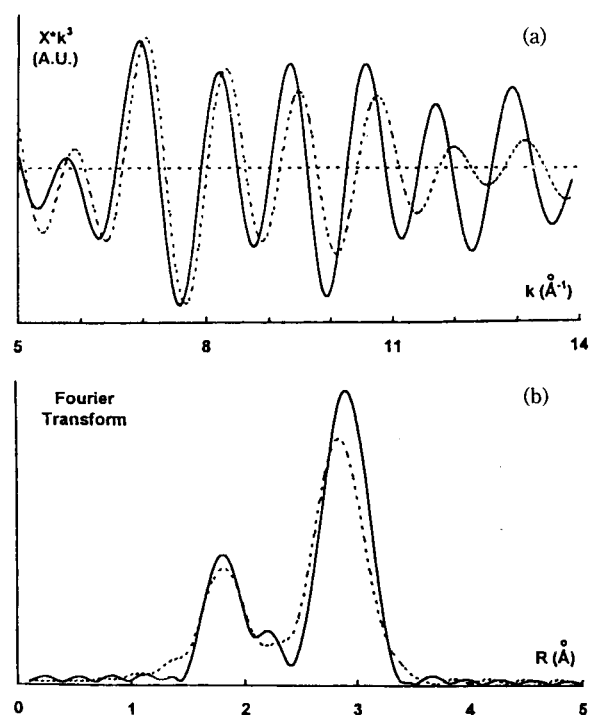
So far there is no explanation of the absence of macroscopic distortion in $Li_{0.98}Ni_{1.02}O_2$. The local distortion of the NiO_6 octahedra is mainly due to a non-cooperative motion of the oxygen and not of the nickel atoms, leading to an unmodified Ni triangular lattice, at least in first approximation. Maybe it is the presence of divalent nickel ions, stable in an isotropic environment, which could hinder the occurrence of a macroscopic distortion.

Table 1. Structural parameter obtained by fitting the EXAFS spectra for the first coordination shell in the framework of the second model used for $Li_{0.98}Ni_{1.02}O_2$

$R_1{}'$ Å	$\sigma_1{}'^2$ ($Å^2$)	$R_1{}''$ (Å)	$\sigma_1{}''^2$ ($Å^2$)	$R_{aver.}$ (Å)	$d_{Ni\text{-}O}$ (Å) Rietveld
1.91	0.008	2.09	0.011	1.97	1.969

Table 2. Structural parameter obtained by fitting the EXAFS spectra for the second coordination shell of $Li_{0.98}Ni_{1.02}O_2$

R_3 (Å)	$\sigma_3{}^2$ (Å)	$d_{Ni\text{-}Ni}$ Å (Rietveld)
2.875	0.009	2.879

$Li_{0.63}Ni_{1.02}O_2$.[26,27] The main goal of the study of $Li_{0.63}$-$Ni_{1.02}O_2$ by EXAFS spectroscopy is to show that the observed monoclinic distortion is not due to a Jahn-teller effect as seen for $NaNiO_2$.
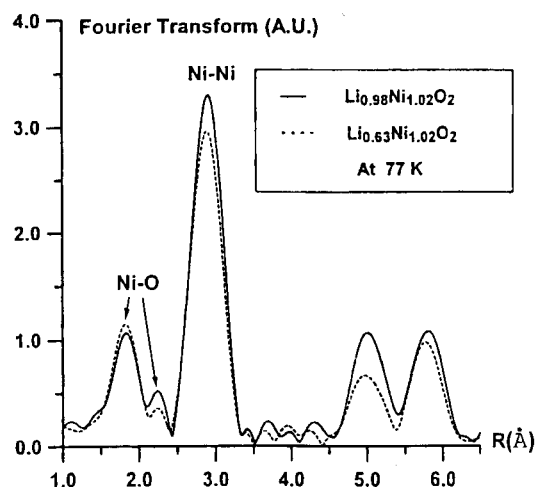
It has been well established that lithium deintercalation from $Li_{0.98}Ni_{1.02}O_2$ leading to $Li_{0.63}Ni_{1.02}O_2$ involves the nickel oxidation from Ni^{III} to Ni^{IV}.

As previously shown the Fourier transform of the Ni-K edge EXAFS signal of $Li_{0.98}Ni_{1.02}O_2$ revealed a well defined splitting of the first peak around 2 Å due to the Jahn-Teller effect of Ni^{3+} in the low spin state. Such a splitting is not observed for $Li_{0.63}Ni_{1.02}O_2$ (Figure 6) at room temperature. This behavior could be due to a hopping phenomenon between $Ni^{IV}(t_{2g}{}^6e_g{}^0)$ and Ni^{III} $(t_{2g}{}^6e_g{}^1)$ which tends to reduce the local distortion. This assumption has been evidenced by recording the EXAFS spectra at liquid nitrogen temperature where the Ni^{III}-Ni^{IV} hopping becomes smaller. The Ni^{III} content (69%) remains high and a local distortion may occur (Figure 9).

To conclude one can say that the monoclinic distortion observed in $Li_{0.63}Ni_{1.02}O_2$ is not due to the Jahn-Teller effect since in this compound the number of distorted NiO_6 octahedra smaller than those observed in $Li_{0.98}Ni_{1.02}O_2$.

The layered oxide $Li_{1-z}Ni_{1+z-t}Fe_tO_2$.[26] This compound belongs to the family characterized by the following general formula:

$$(Li_{1-z}Ni_z^{II})(Ni_z^{II}Ni_{1-z-t}^{III}Fe_t^{III})O_2$$

X-Ray Absorption Spectroscopy

Bull. Korean Chem. Soc. **1998**, Vol. 19, No. 1   11

Figure 9. Experimental Fourier transforms for Ni K-edge EXAFS of $Li_{0.98}Ni_{1.02}O_2$ and $Li_{0.63}Ni_{1.02}O_2$ phases, at liquid nitrogen temperature.

The study of the iron-based lithium nickel oxide is made in the framework of the improvement of the positive electrode in Li-rechargeable batteries. Several cationic substitutions have been used as for example Al/Ni, Fe/Ni and Co/Ni. Only the Ni/Co substitution has clearly improved the performances of the positive electrode by increasing the amount of lithium intercalated in the oxide and by decreasing the polarization of the batteries.[24,28] The substitutions with Al and Fe were unsatisfactory. In order to understand why the Ni-Fe substitution has rather a negative effect, a structural characterization has been undertaken by using X-ray diffraction (Rietveld method), EXAFS and Mössbauer spectroscopies.

For $t < 0.30$ the oxides are isostructural with $Li_{1-z}Ni_{1+z}O_2$. As for the other lithium nickel oxides the Rietveld refinement shows an electron deficiency at the lithium sites, suggesting the presence of Ni/Fe cations in the lithium sites.

At this stage of the study two main questions were raised (i) what is the oxidation state of iron cations. (ii) where are located iron cations.

Magnetic measurements and Mössbauer spectroscopy study have shown that iron is in a trivalent state with a high spin configuration for $Li_{.1}Ni_{0.90}Fe_{0.10}O_2$.

The Mössbauer resonance spectrum recorded at room temperature exhibits a quadrupolar doublet which is characteristic of the trivalent iron in a regular octahedral site (O_h) (Figure 10). The values of both the isomer shift and the quadrupolar splitting (δ=0.33 mms^{-1} and Δ=0.33 mms^{-1}) are very close to those found in the isostructural compound α-NaFeO$_2$ (δ=0.35 mm and Δ=0.45 mms^{-1}).[29] This observation which leads to the presence of Fe^{III} in NiO$_2$ slabs is in disagreement with a previous study for which the authors claimed, from a X-ray anomalous diffusion study, that Fe^{III} cations were located in the interslab space corresponding to the lithium sites.[30]

In order to settle the problem of the location of Fe^{III} in the structure, EXAFS experiments have been carried out on $Li_{.1}Ni_{0.80}Fe_{0.20}O_2$ at both the Ni-K edge and the Fe-K edge with the same experimental conditions used previously for $Li_{0.98}Ni_{1.02}O_2$.
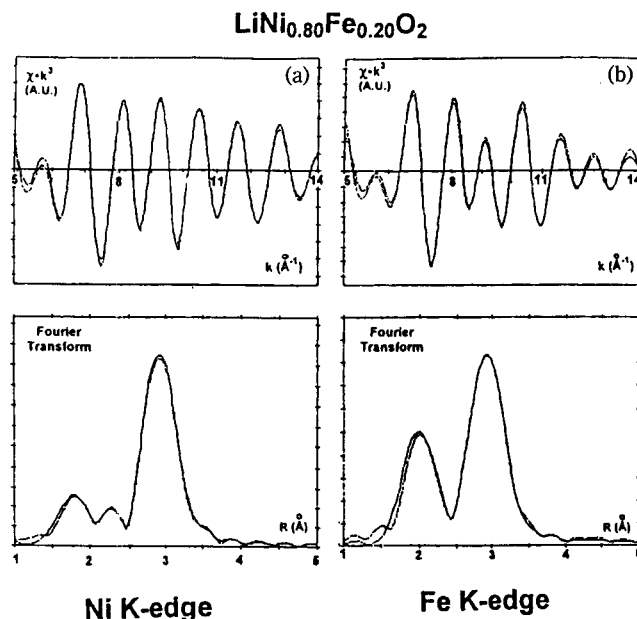
Weighted k^3 EXAFS spectra and filtered Fourier trans-
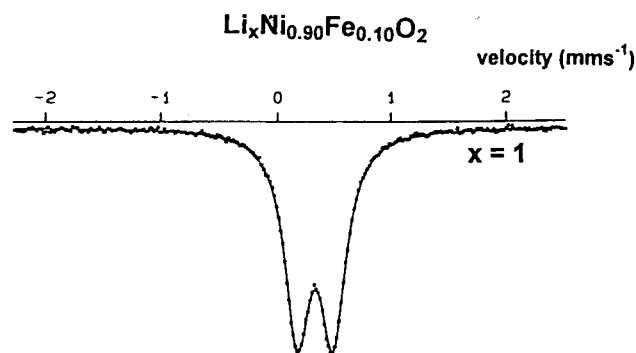
$$LixNi_{0.90}Fe_{0.10}O_2$$

Figure 10. Mossbauer spectrum of $LixNi_{0.90}Fe_{0.10}O_2$ recorded at room temperature.

forms (Figure 11) show that Ni^{III} is located in distorted octahedral sites with four short and two long Ni-O bond lengths and Fe^{III} is in regular octahedral sites (d_{Ni-O}=2.012 Å from EXAFS measurements and d_{Ni-O}=1.983 Å from Rietveld refinement).
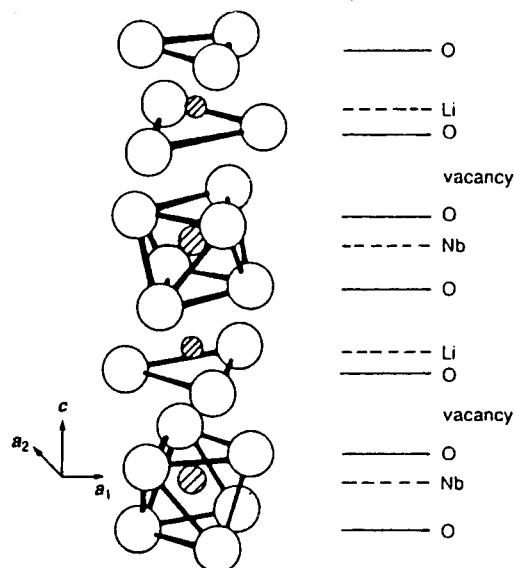
For respecting the charge compensation, the divalent nickel cations Ni^{II} are equallized in both NiO$_2$ inter- and intraslab spaces.

It is worthwhile noting that in all the EXAFS studies performed at the Ni-K edge of the layered oxides (Li_{1-z} $Ni_z{}^{II}$) ($Ni_z{}^{II}$ $Ni_{1-z}{}^{III}$) O$_2$, four short and two long bond lengths have been evidenced. Due to the small amount of Ni^{II} cations in these oxides (<10%), the two different distances which are observed result from the distortion of the NiO$_6$ octahedra are cannot be attributed to the simultaneous presence of Ni^{III} et Ni^{II}.

Location of cation dopants in oxides.[31] LiNbO$_3$ and LiTaO$_3$ crystals exhibit a photorefractive effect and have important applications in non-linear optical storage and phase conjugation devices.[32-35] The photorefractive properties are closely related to the nature of the impurities or lattice defects in the crystals. Many techniques were used

$$LiNi_{0.80}Fe_{0.20}O_2$$

Ni K-edge   **Fe K-edge**

Figure 11. k^3 weighted absorption spectra $\chi(k)$ and filtered Fourier transforms (a) at the Ni K-edge (b) at the Fe K-edge.

12 *Bull. Korean Chem. Soc.* **1998**, Vol. 19, No. 1

Jean Etourneau

Figure 12. Schematic representation of the crystal structure of LiNbO₃.[31]

Figure 13. Fourier transform of the Fe K-edge EXAFS in 6 mol% doped LiNbO₃. The data have been Fourier filtered over the range 1-4 A. The solid line is the experiment and the dashed line the theoretical fit.[31]

for determining the location of transition metal impurities. For reaching this goal a lot of techniques have been used such as EPR, optical and Mössbauer spectroscopies.[32-34,36,37]

Figure 12 gives a schematic representation of the structure of LiNbO₃ (R_{3c} Space group) which derives from the corindon one. Lithium and niobium are located in octahedral sites. The octahedra are corner-sharing for a same cation Li⁺ or Nb⁵⁺.

The problem which is raised concerns the location of the impurities. Among the techniques used for situating the impurities in the structure, EXAFS spectroscopy is one of the best, since it gives a direct information of the nature of the nearest cation shell. For instance if the impurity is on a Li⁺ site, the shell of nearest neighbour cations will contain Nb⁵⁺ cations which are strong backscatterers. In this case prominent peaks should occur in the Fourier transform. In inverse order, the location of the impurity at the Nb⁺⁵ site will lead to low intensity peaks for the second shell containing weak Li⁺ backscafferers.

According to these observation, the preference is for the Li⁺ site as host for the impurities like Mn²⁺, Fe³⁺, Eu³⁺, Nd³⁺, Ti⁴⁺, Ni²⁺. However Eu³⁺ and Nd³⁺ and even Fe³⁺ for a minor fraction, can occupy Nb⁵⁺ site.

The doping of LiNbO₃ by Fe³⁺ cations (6 mol%) has been chosen as an example for demonstrating the interest of EXAFS spectroscopy for knowing the nature of the cation site (Li⁺ or Nb⁵⁺) occupied by the dopants.[31] A simple crystal chemistry reasoning allows to conclude that the location of Fe³⁺ in Li⁺ site should show that Fe³⁺-O distances are shorter than the Li⁺-O ones. Conversely the location of Fe³⁺ in Nb⁵⁺ site should show that Fe³⁺-O distances are longer than the Nb⁵⁺-O ones.

The strong peaks which occur in the Fourier transform of the Fe-K edge of the EXAFS spectrum (Figure 13) in the region 3-4 Å shows clearly that Fe³⁺ ions occupy the Li⁺ sites. This is confirmed by the detailed least-squares fitting of the EXAFS signal which shows that the Fe³⁺-O distances are shorter than the Li⁺-O ones as indicated in Table 3 for the
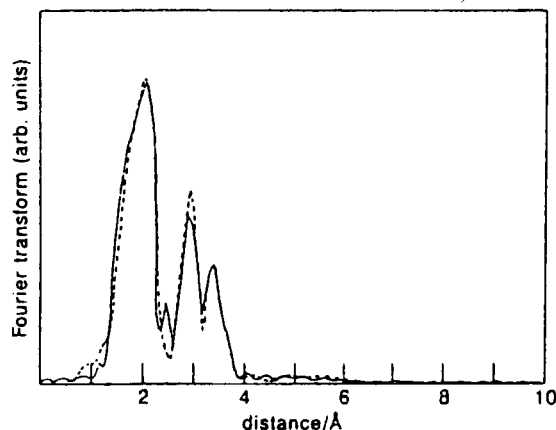
three oxygenated shells surrounding Fe³⁺.

Characterization of copper pairs in NASICON-type phosphate Cu^I Zr₂(PO₄)₃ by EXAFS. The NASICON-type phosphate Cu^I Zr₂(PO₄)₃ exhibits remarkable properties in two different fields of material science. On one hand it is an active catalyst of 2-butanol decomposition with a periodic oscillatory behavior;[38] on the other hand this phosphate is the first example of a Cu-rich insulating phosphor: under UV excitation blue and green fluorescences are observed respectively at low and room temperatures.[39]
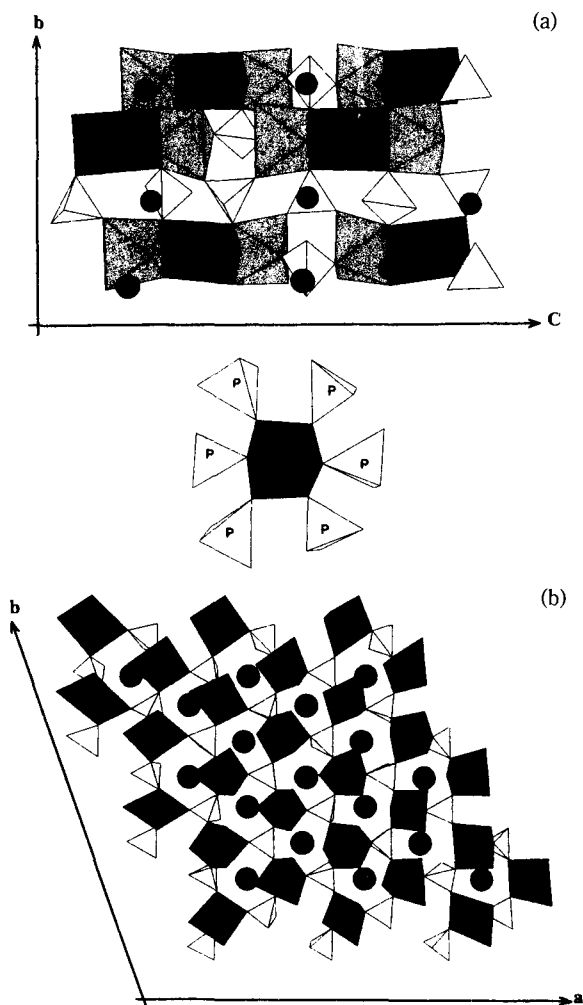
In order to explain the mechanisms involved in both catalytic and optical properties it was of interest to investigate in details the crystal structure of Cu^I Zr₂(PO₄)₃. In a first approximation, the structure of the NASICON-type phosphates, whose prototype is NaZr(PO₄)₃, consists of a three dimensional network formed by PO₄ tetrahedra sharing corners with ZrO₆ octahedra as shown in Figure 14. The site occupied by sodium is an elongated antiprism formed by triangular faces of two ZrO₆ octahedra along the c-axis of the hexagonal cell. This site is usually called M₁. The framework creates also a large ten-fold coordinated site M₂. Every M₁ site is surrounded by six M₂ sites sharing common triangular faces.

The structural studies of Cu^I Zr₂(PO₄)₃ were motivated by its luminescent properties observed in a wide temperature range. At 6 K the optical spectrum displays an excitation band peaking at 270 nm and a blue fluorescence band with a maximum of intensity at around 410 nm. As the temperature increases a new fluorescent band progressively arises with a maximum at 540 nm; correlatively a broad shoulder appears on the low energy side of the excitation band which concerns only the green emitters.[40] Thus the

Table 3. Structural parameters obtained by fitting the EXAFS spectra of lithium niobate

Shell	Atom type	Coordination number	Bond distances (Å)		σ² (Å²)
			LiNbO₃:Fe³⁺	pure LiNbO₃	
1	0	3	1.985	2.068	0.013
2	0	3	2.028	2.238	0.024
3	0	3	3.046	3.287	0.004

X-Ray Absorption Spectroscopy

Bull. Korean Chem. Soc. **1998**, Vol. 19, No. 1   13


Figure 14. (a) Schematic representation of the Nasicon-type structure [*e.g.* CuZr₂(PO₄)₃]. Projection onto the b, c plane and surrounding of the M₁ site. (b) Schematic representation of the Nasicon-type structure Ce.g. CuZr₂(PO₄)₃]. Projection onto the a, b plane.

unusual luminescent properties of $Cu^IZr_2(PO_4)_3$ suggested the existence of two types of emitting centers involving copper.

X-ray and neutron diffraction experiments were firstly performed on both $CuZr_2(PO_4)_3$ and $CuTi_2(PO_4)_3$. Copper atoms are located in M₁ site and statistically distributed between six off-centered equivalent positions (36 f) with a statistical occupancy (1/6); the distance between the symmetrical positions in the lattice being is very small in the case of $CuTi_2(PO_4)_3$ (1.59 Å) and noticeably larger for the zirconium phosphate (2.25 Å).[41]

At first sight the coexistence of two Cu atoms within the same M(1) seemed to be unrealistic. Nevertheless, as already reported, the two fluorescence bands of $CuZr_2(PO_4)_3$ observed at room temperature arise clearly from two distinct excitation centers,[39] Both X-ray and neutron diffraction experiments cannot account of the existence of two crystallographic sites for the Cu ion.

However, as described previously, various fluorescent Cu^I complexes show low-energy emissions with their maximum located between 550 and 628 nm as Cu^I-Cu^I distances are
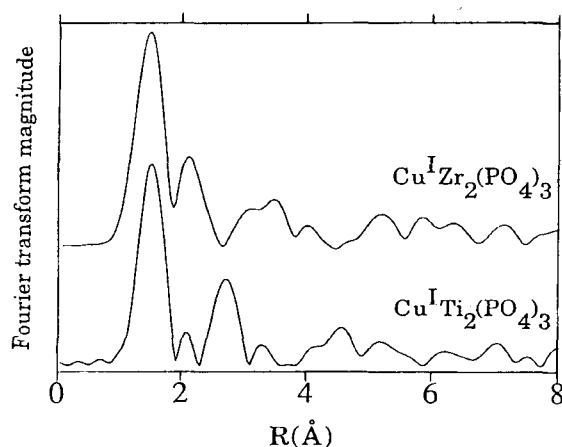
Figure 15. Radial structure functions, uncorrected phase shift for $CuTi_2(PO_4)$, and $CUZra_2(PO_4)_3$. The first major peak is attributed to first-neighbour oxygen atoms and its amplitude reflects the number of first-shell oxygen atoms surrounding Cu. The second peak is attributed to second-shell atoms surrounding the Cu: copper and oxygen atoms for $Cu^IZr_2(PO_4)_3$, Oxygen atoms only for $Cu^ITi_2(PO_4)_3$.

smaller than 2.8 Å.[42] According to theoretical calculations, Cu^I-Cu^I interactions should exist.[43,44]

The problem was to show the possible existence of Cu^I-Cu^I pairs in $CU^IZr_2(PO_4)_3$ by performing EXAFS experiments. For the sake of comparison the EXAFS analysis was carried out by using standard methods in the plane wave approximation for both $Cu^ITi_2(PO_4)_3$ and $Cu^IZr_2(PO_4)_3$.[45,46] Cu $_2O$ has been taken as a reference compound for determining the phase shifts and the backscattering amplitudes.
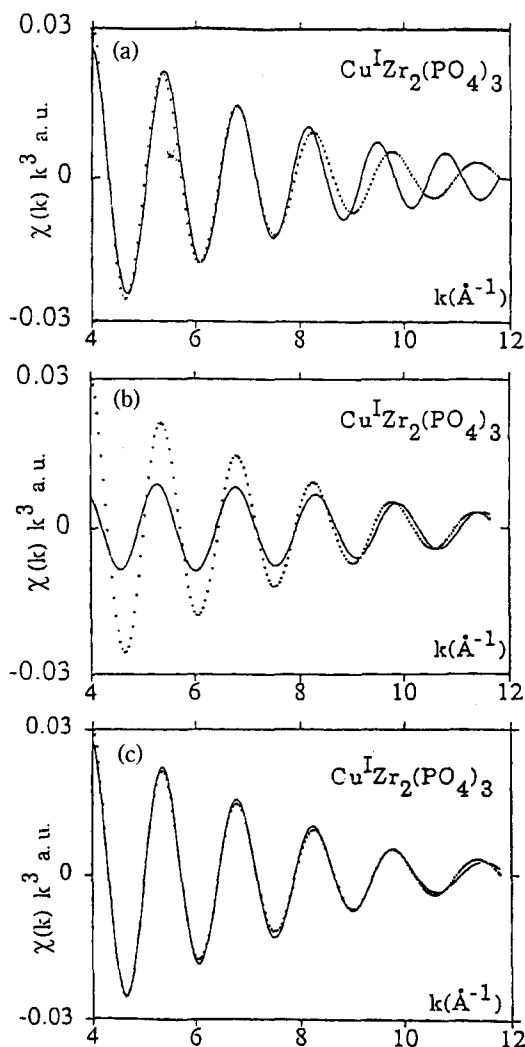
The radial structure functions of the Cu K-edge EXAFS spectra given in Figure 15 show different peaks corresponding to individual coordination shells.

In the first shell with Cu as central atom, two oxygen atoms are found for both compounds, as it is usually observed for Cu^I oxides. The Cu-O distances ($\cong 2$ Å) are slightly less than those reported from X-ray or neutron diffraction experiments: 2.08 Å (X-ray) and 2.06 Å (neutron) for $CuTi_2(PO_4)_3$; 2.05 Å (X-ray) and 2.09 Å (neutron) for $CuZr_2(PO_4)_3$.[41,47]

The second peak attributed to the second shell surrounding copper consists of copper and oxygen atoms for $Cu^IZr_2(PO_4)_3$ and oxygen atom only for $Cu^ITi_2(PO_4)_3$.

The EXAFS simulation relative to the second shell around copper for $Cu^IZr_2(PO_4)_3$, indicates the presence of 1.6 oxygen atoms at 2.73 Å from the copper central atom and 0.4 copper pairs exhibiting a short distance: 2.40 Å. As shown in Figure 16, the EXAFS signal cannot be fitted without introducing Cu^I-Cu^I pairs in the second shell. This can be demonstrated by comparing the EXAFS functions generated by Fourier back transforming the second peak of the radial structure, with least-squares fits obtained for different atomic compositions of the second shell: Figure 16a (only 1.64 0); Figure 16b (only 0.4 Cu); Figure 16c (1.64 O+0.4 Cu).[45]

Thus, the EXAFS simulation of the second shell gives an estimation of the number of M1 sites occupied by copper. Since the number of M1 sites is equal to the number of copper atoms, 0.2 M1 site are occupied by (Cu⁺)₂, 0.6 M1

Figure 16. EXAFS function generated by Fourier back-transforming the second peak of the radial structure function for Cu in $Cu^IZr_2(PO_4)_3$ (crosses) compared with least-squares fits obtained with the following second-neighbour atoms (solid lines): a, only 1.64 O; b, only 0.4 Cu; c, 0.4 Cu and 1.64 O, in the second shell of central Cu.

site are occupied by single Cu^+ ion and therefore 0.2 M1 site are empty. In contrast for $CuTi_2(PO_4)_3$, the smaller size of the M1 site prevents the formation of copper pairs.

The existence of copper pairs has been indirectly evidenced by examining the optical properties of different oxygenated materials through the STOKES shift as a function of the excitation energy for isolated and paired copper ions (Figure 17), While all the compounds containing $(Cu^+)_2$ exhibit a similar stokes shift, resulting from a quasi-constant Cu-Cu distance in the host matrix, those containing isolated Cu^+ ion show a STOKES shift which depends strongly on the local structure.

Characterization of local structures in glasses

As already mentioned a valuable feature of the XAS technique is that it does not account of long range order in the material and thus can be used to probe local structure in both crystalline and amorphous solids. Recent reviews cover the use of the technique in the structural investigation of glasses.[49,50]
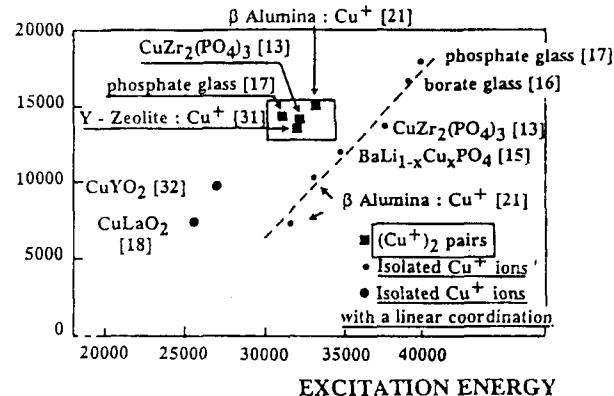
Figure 17. Stokes shift as a function of excitation energy for various copper activated oxygenated insulators in a crystallitzed or glassy state.

To show the interest of both XANES and EXAFS for characterizing glasses we have chosen three systems exhibiting non-linear optical properties for the development of new materials for ultra-fast switching or signal processing.[51] According to a semi-empirical model the materials able to show non-linear properties with a high non-linear index n_2 would be those exhibiting hyperpolarization chemical bonds or structural entities.[52] The purpose of the present study is to characterize the local environment of titanium or tellurium in oxygenated glasses and to relate the observations made with the non-linear optical properties of the materials. It will be shown that Raman spectroscopy in combination with the XAS one is a complementary technique for characterizing glasses.

TiO, in various silicate and borophosphate glass matrixes.[53,54] Raman scattering and X-ray absorption studies have been carried out on non-linear otpical glasses having the composition: $xTiO_2$, $yNaPO_3$, $zNa_2B_4O_7$. As a general rule, the non-linear refractive indices increase with TiO_2 content. According to a previous work,[52] rutile finds its high non-linearity in the hyperpolarizability of the Ti-O bond. Therefore the nature of local environments around titanium atoms in glasses was necessary to know in order to make correlations between the observed titanium sites geometry and the measured non-linear response.

Experimental procedures and the conditions used in both Raman and XAS spectroscopies are detailed elsewhere.[53,54] Here, the conclusions of the studies will be reported.

In Raman spectroscopy Ti-O vibrations are identified by four specifie broad bands (Figure 18) at around:

$-930\ cm^{-1}$ (band a) corresponds to the ν(Ti-O*) vibration where O* denotes an apical oxygen in a squared pyramidal environment of Ti.

$-740\ cm^{-1}$ (band b) which proves the presence of --Ti-O-Ti-O-Ti-- chains where short Ti-O bonds alternate with long Ti-O ones as already seen in other compounds KTi-OPO$_4$ (KTP) and $NaTiOPO_4$ crystals.[55,56] It appears that short Ti-O* bonds vanish with the formation of Ti-O-Ti chains.

-640 and $500\ cm^{-1}$ (band c and d) could be the signature of distorted TiO_6 octahedra by referring to the previous analysis of $BaTiO_3$ and K_2NiF_4 fype titanates.[57,58]

Complementary information has been brought by XANES

X-Ray Absorption Spectroscopy

*Bull. Korean Chem. Soc.* **1998**, Vol. 19, No. 1 15
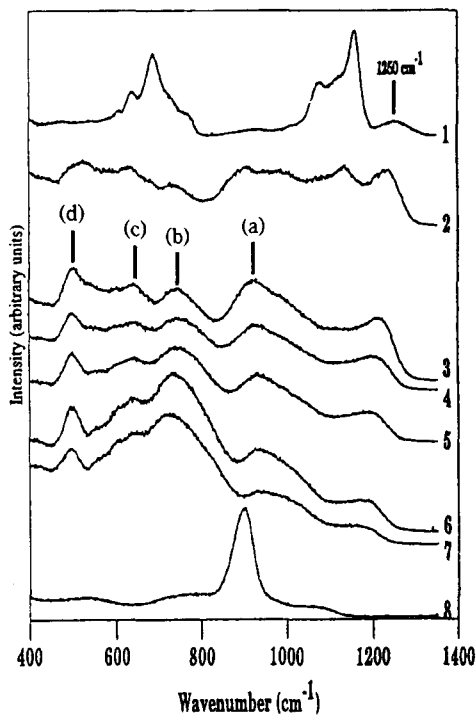
Figure 18. Raman spectra of $x\text{TiO}_2(1-x)$ [$0.05\text{Na}_2\text{B}_4\text{O}_7$, 0.95 NaPO_3] glass samples of compositions $x=0(1)$; $x=15.0$ (2); $x=26.3$ (3); $x=29.0$ (4); $x=33.3$ (5); $x=38.5$ (6); $x=42.2$ (7) and $\text{K}_2\text{O-TiO}_2$-2SiO_2 silicate glass.

and EXAFS studies. By using reference compounds XANES analysis (Figure 19) show clearly from the pre-edge peak positions which can be unambiguously compared each other since the energy differences between different Ti site symmetry features remain beyond experimental error. TiO_2 anatase, Ba_2TiO_4 and $\text{K}_2\text{O-TiO}_2$-2SiO_2 glass are representative of octahedral, tetrahedral and square-based pyramidal geometries respectively. For example, each borophosphate glass spectrum (Figure 19) shows a single pre-edge peak with shoulders on each side, which is the signature of square-based pyramidal sites. By a proportionality process using the height of the corresponding peak from the silcate reference glass, one can roughly deduce the rate of this type of site in borophosphate
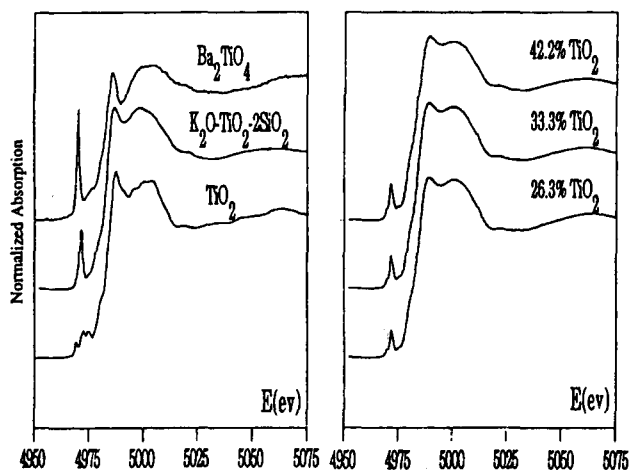
Figure 19. Ti K-edge XANES spectra of borophosphates glasses and reference compounds.
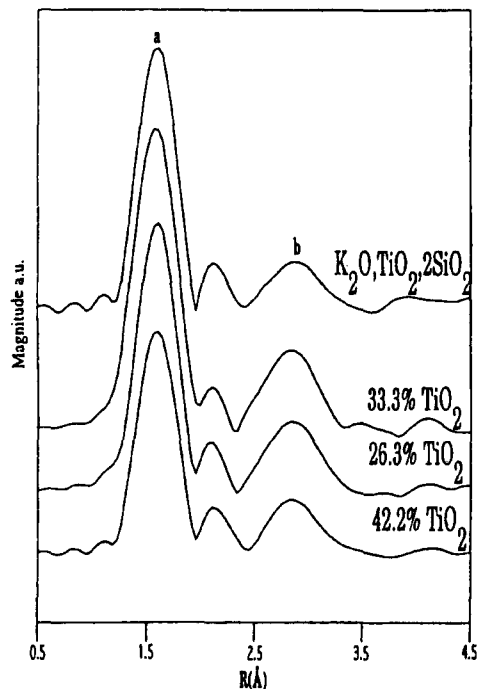

Figure 20. Fourier transforms uncorrected for phase shift for three compositions of borophosphate glasses and the potassium silicate reference glass a an b point to the first and second shell, respectively.

glasses. Square-based pyramidal sites increase with TiO_2 content which is in agreement with Raman studies. With respect to XANES and Raman studies, EXAFS investigation (Figure 20) have allowed to precise not only the symmetry of the titanium sites but also the values of the Ti-O bond distances by fitting the EXAFS first shell experimental signals with adjustable parameters as the edge energy E_0 which is allowed to vary for simulations in view of ensuring the transferability of the tabulated parameters (amplitude and phase functions of the backscattered atoms), the electron mean free path $\lambda_{(k)}=\dfrac{k}{\Gamma}$

where is a fitting parameter, σ^2 the Debye Waller factor and two Ti-O distances resulting from the presence of two different type of sites already identified by XANES and Raman studies; the number of oxygen neighbours N was fixed (six for anatase; four in the plane square of pyramidal sites and one in the axial direction for the silicate glass). From the EXAFS study itself we cannot decide between the presence of TiO_5 tetragonal pyramids with a short axial titanyl bond Ti-O or distorted TiO_6 octahedra. In fact both sites are present in the borophosphates. However by combining Raman spectroscopy, XANES and EXAFS data one can conclude that there is an original structural organization of Ti-O_5 sites in the borophospahtes, exhibiting a short Ti-O bond whose hyperpolarizability would be responsible for the non-linear properties of the materials.[59]

Tellurites glasses.[60] The interest for studying tellurite glasses results mainly for their promising electrical and non-linear optical properties and furthermore they exhibit high values of both linear and non-linear indices, low melting temperature and wide infrared transmittance.[61,62] For example the non-linear refractive index n_2, found in TeO_2-Nb_2O_5 glasses, is 40 times larger than that observed for SiO_2.[63] In

TeO₄ tbp   **TeO₃₊₁ polyhedron**
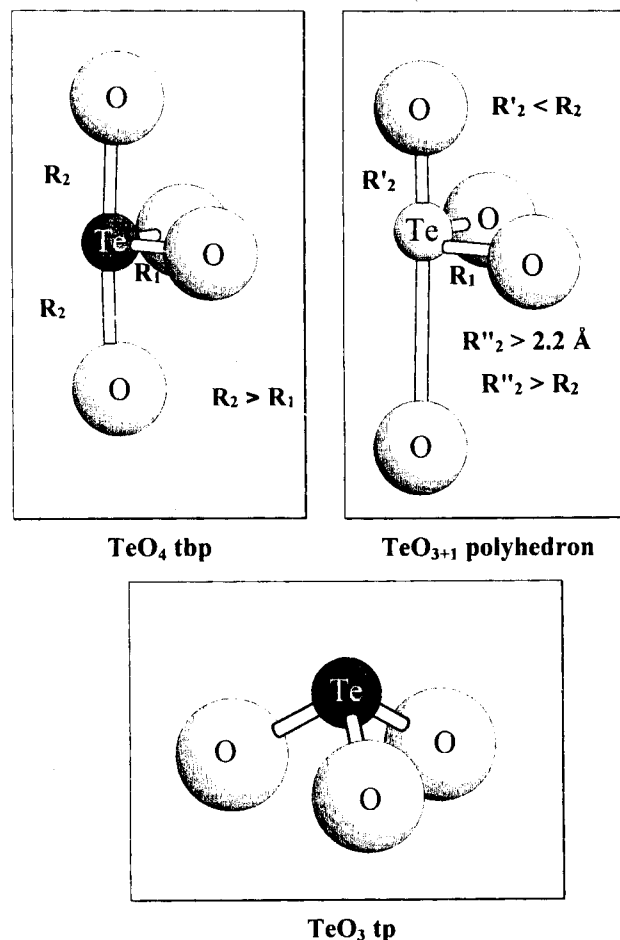
TeO₃ tp

Figure 21. Representation of the tellurium atom coordination by oxygen atoms: TeO_4 trigonal bipyramid tbp; TeO_{3+1} asymmetric polyhedron; TeO_3 trigoral pyramid (tp).

order to understand such a behavior, the local structure of both TeO_2-Nb_2O_5 and TeO_2-Al_2O_3 oxide glasses has been investigated by XANES and EXAFS spectroscopies and the results obtained have been compared with those deduced from Raman spectroscopy.[63,64] The origin of the pre-edge peak in the XANES study has been determined by *ab-initio* calculations.

In Te-based oxygenated compounds three TeO_n entities can be observed (Figure 21): (i) a TeO_4 somewhat trigonal bipyramid (tbp) (ii) a TeO_{3+1} asymmetric polyhedron in which one Te-O axial bond is shorter while the other is longer with respect to which is observed for TeO_4 (iii) a TeO_3 trigonal pyramid (tp) with three short Te-O distances.

For Raman, XANES and EXAFS spectroscopies, reference compounds have been investigated as (i) α-TeO_2 which exhibits distorted TeO_4 (tbp) entity (ii) $ZnTeO_3$ which shows TeO_3 (tp) entity.[60,63,64] The experimental conditions used for recording and simulating the different spectra, are given in details in ref. 60.

All XANES spectra recorded at the Te-L_{III} edge (Figure 22) exhibit pre-edge peaks P_1 whose energy positions are comparable. However a zoom on this pre-edge peak shows structural differences depending on the compounds. For a $ZnFeO_3$ crystal, only one well-defined peak is observed, whereas for α-TeO, a quite significant shoulder P_2 appears
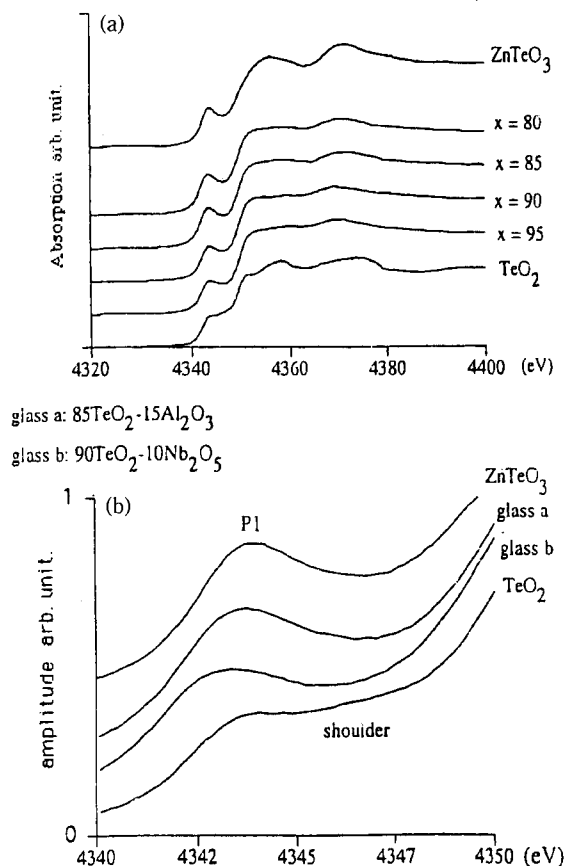
Figure 22. (a) Te-L_{III} edge XANES spectra of $xTeO_2$-$(1-x)Al_2O_3$ and reference crystals (b) Zoom of the pre-edge peak.

exactly at the beginning of the slope of the edge, around 3 eV after the maximum of the peak P_1. An intermediate feature tends to look like more and more that of $ZnTeO_3$ with increasing Al_2O_3 or Nb_2O_5 content. These first results are in agreement with those deduced from Raman spectroscopy studies,[63] indicating that both TeO, and TeO_{3+1} clusters are present in glasses. In other words Raman and XANES experiments indicate the transformation of some entities into TeO_{3+1} ones as the rate of TeO_2 content decreases in glasses.

From *ab-initio* molecular orbital calculations made in the restricted Hartree-Fock scheme (RHF) for TeO_4^{4-} and TeO_3^{2-} clusters (Figure 23), it has been shown in both cases that the highest occupied orbital a* (HOME) is of antibonding character and combines essentially 5 s AO of Te and 2p of oxygen atoms. A part of this orbital is localized on tellurium and oriented towards the external side of the clusters; the electrons filling this orbital should be considered as highly polarizable. Due to the fact that the polarizability proceeds from an electric field dipolar moment coupling between the highest occupied molecular orbital (HOME) and the lowest unoccupied molecular orbital (LUMO), it is expected that the polarizability is all the more important as the energy gap between HOME and LUMO is smaller. Consequently the antibonding electron doublet should be less polarizable for TeO_3^{2-} than for TeO_4^{4-} and thus the linear and the non-linear index values should be higher with materials containing TeO_4 clusters. Furthermore al these results

X-Ray Absorption Spectroscopy

Bull. Korean Chem. Soc. **1998**, Vol. 19, No. 1 17
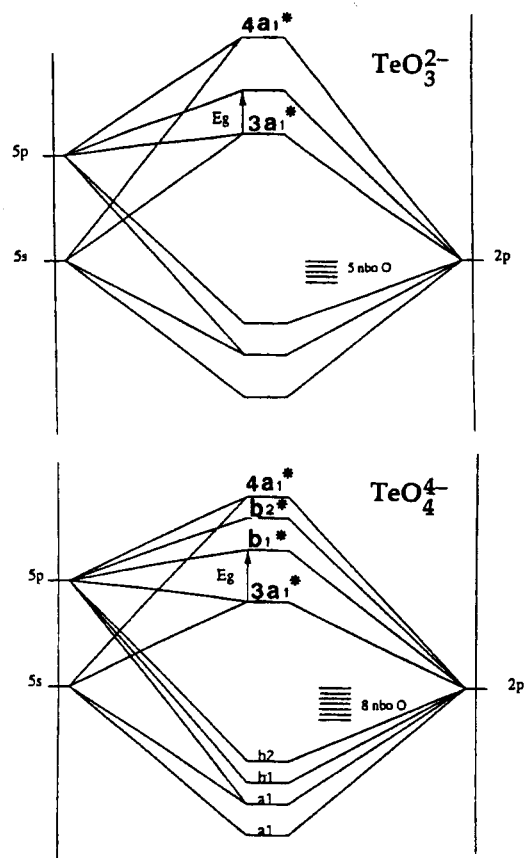
Figure 23. Qualitative molecular orbital diagram of TeO_3^{2-} and TeO_4^{4-} entities (nbo O:nonbonding orbitals of oxygen atoms; Eg: energy difference between HOME and LUMO).

suggest that the origin of the pre-peak P_1 corresponds to the transition $2p_{3/2}$ $4a_1$* (the third vacant antibonding molecular orbital). So far, no explanation has been found for justifying the presence of a shoulder in the XANES spectrum of α-TeO_2.

From RAMAN and XANES spectroscopy experiments it has been shown that in all investigated glasses, the tellurium environment consists of TeO_4 trigonal bipyramidal polyhedron and TeO_{3+1}-type polyhedron and furthermore the addition of Al_2O_3 or Nb_2O_5 increases the proportion of the asymmetric entity TeO_{3+1}.

EXAFS spectra have been recorded (*e.g.* of 85 TeO_2-15 Al_2O_3 in Figure 24) at the Te-K edge and for their simulation both structural entities have been taken into account. For the first oxygen shell are considered (Figure 21): two short equatorial distances (R_1), the shortest axial distance (R_2, R_2) and the elongated axial bond $R_2^{''}$. Assuming that the proportion of TeO_4 and TeO_{3+1} clusters are respectively (1-x) and x, the number of equatorial distances N_1 is 2 whereas the number of axial distances N_2 is included between 1 and 2, depending on the additional oxide rate and assuming that the elongated axial bond gives an evanescent EXAFS signal. Due to the low accuracy of the EXAFS simulation on the number of atoms in the shell (less than 30% error) as well as the high correlation with σ^2, a realistic estimation of both N_1 and N_2 has been excluded and for the fitting N_1 and N_2 equals 2 for each. As expected the EXAFS data show clearly that the equatorial bond lengths
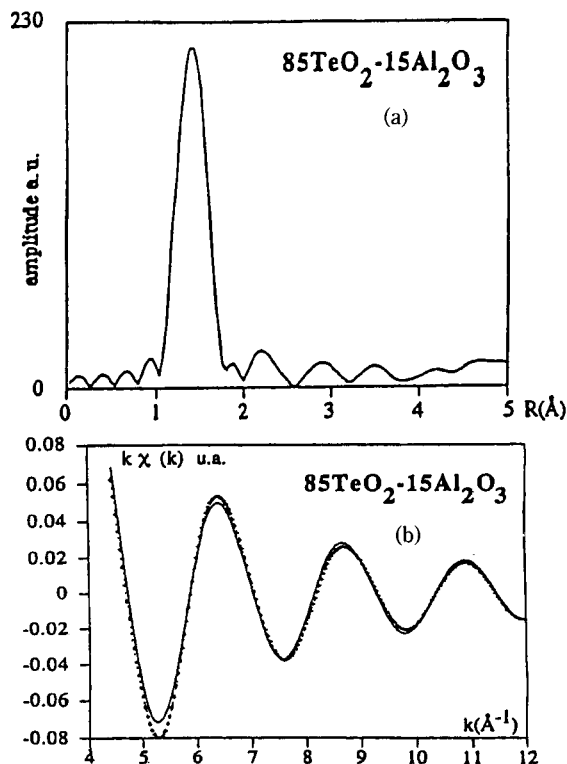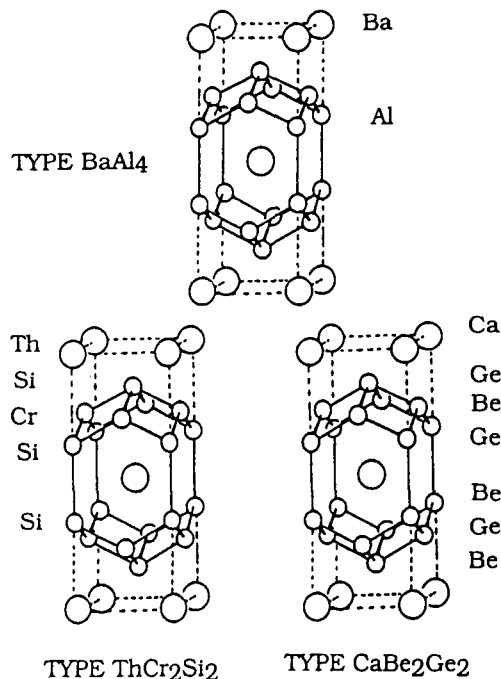

Figure 24. (a) Fourier transform of 85TeO$_2$-15Al$_2$O$_3$ glass (first oxygen shell) (b) Experimental and simulated Te K-edge EXAFS spectra of 85TeO$_2$-15Al$_2$O$_3$ glass (first oxygen shell).

remain practically constant (1.88-1.90 Å) whereas the average axial distances decrease either with an increase of Nb_2O_5 content (from 2.06 Å down to 2.00 Å) or with an increase of Al_2O_3 content (from 2.07 Å down to 2.01 Å).[60] This observation is consistent with a progressive transformation of TeO_4 polyhedra into asymmetric TeO_{3+1} ones.

Characterization of the electronic structure of solids: study of the cerium valence state in ternary silicides.[65] The ternary silicides REIr$_2$Si$_2$ (RE: rare earth) have two allotropic varieties. At low temperature they crystallize in the ThCr$_2$Si$_2$-type structure (space group I4/mmm) which is adopted by several other ternary silicides such as REM$_2$Si$_2$ with M=Fe, Ru, Os, Co, Rh. The stable form at high temperature is isostructural with CaBe$_2$Ge$_2$ (space group P4/nmm).[66] Both structural types are ordered ternary derivatives of the binary BaAl$_4$-type structure (Figure 25).

The physical properties of the silicides REIr$_2$Si$_2$ are strongly influenced by their crystal structure. For example, in the CaBe$_2$Ge$_2$-type structure, LaIr$_2$Si$_2$ and YIr$_2$Si$_2$ are superconducting at 1.6 K and 2.45 K respectively.[67,68] On the contrary, in the ThCr$_2$Si$_2$-type structure, LaIr$_2$Si$_2$ is not superconducting above 1 K and YIr$_2$Si$_2$ shows only an onset of superconductivity around 2 K. Similarly, it has been shown that correlations exist in these silicides between magnetic and structural properties: in the case of TbIr$_2$Si$_2$, the Neel temperatures of the low and high temperature modifications are 80 K and 13 K respectively.[69] The variety of the observed superconducting and magnetic behaviors of the REIr$_2$Si$_2$ silicides results likely from the influence of the different three-dimensional Ir-Si skeletons on the density of states at Fermi level.
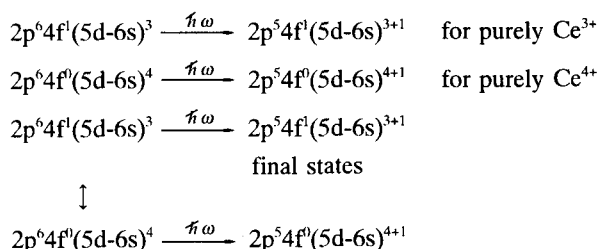
18 *Bull. Korean Chem. Soc.* **1998**, Vol. 19, No. 1

Jean Etourneau

TYPE BaAl4

Ba

Al

Th
Si
Cr
Si

Si

Ca
Ge
Be
Ge

Be
Ge
Be

TYPE ThCr2Si2

TYPE CaBe2Ge2

Figure 25. Perspective of the structure of $ThCr_2Si_2$ and $CaBe_2$ Ge_2 deriving from $BaAl_4$-type structure.

According to the structure in which cerium is embeded and the nature of the components of the host matrix, cerium can exhibit different electronic ground state: $Ce^{3+}[4f^1(5d6s)^0]$, $Ce^{4+}[4f^0(5d6s)^0]$ and an intermediate valence state for which the 4f level pinned at the Fermi level and the 5d-6s delocalized states are degenerate $[4f^1 (5d-6s)^3 \leftrightarrow 4f^0(5d-6s)^4]$.

The Ce-based ternary silicides with the general formulae CeT_2Si_2 with T=Ru, Os, Co, Rh, Ir, have been chosen for showing that magnetic and electrical measurements are complementary to XANES studies at the L_{III} edge for characterizing the electronic state of cerium.[65,70]

Very schematically one can say that the electronic transitions which are involved at the L_{III} absorption edge of cerium are:

$$2p^6 4f^1 (5d\text{-}6s)^3 \xrightarrow{\hbar\omega} 2p^5 4f^1 (5d\text{-}6s)^{3+1} \quad \text{for purely } Ce^{3+}$$

$$2p^6 4f^0 (5d\text{-}6s)^4 \xrightarrow{\hbar\omega} 2p^5 4f^0 (5d\text{-}6s)^{4+1} \quad \text{for purely } Ce^{4+}$$

$$2p^6 4f^1 (5d\text{-}6s)^3 \xrightarrow{\hbar\omega} 2p^5 4f^1 (5d\text{-}6s)^{3+1}$$

final states

$$\updownarrow$$

$$2p^6 4f^0 (5d\text{-}6s)^4 \xrightarrow{\hbar\omega} 2p^5 4f^0 (5d\text{-}6s)^{4+1}$$

On the XANES spectra, recorded at both room temperature and Ce L_{III}-edge, occurs a main line assigned to $4f^1$ and in addition in the case of fluctuating compounds, a high energy satellite due to the $4f^0$ final state configuration (Figure 26). In valence fluctuating rare earth compounds, one should have to notice that the replicate splitting due to the two possible configurations when the passive electrons are included, is 8-9 eV, equal to the energy by which the 4f level is lowered by the core hole.[71]

Magnetic susceptibility measurements (Figure 27) and electrical measurements (Figure 28) performed in a large
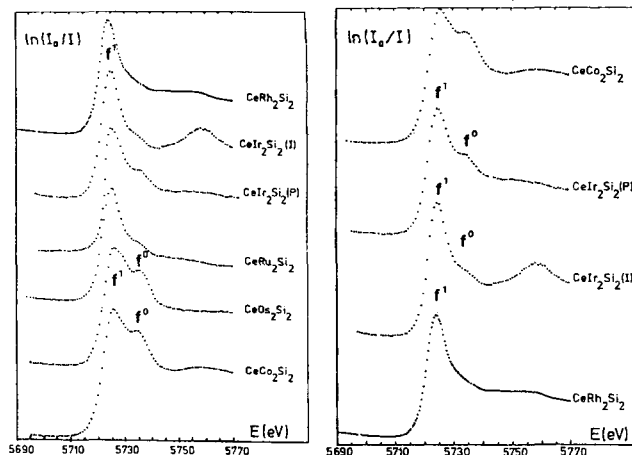
Figure 26. CeLIII-edge XANES spectra of CeT_2Si_2 silicides with T=Ru, Os, Co, Rh, Ir [(P)CaBe$_2$Ge$_2$-type; (I) ThCr$_2$Si$_2$-type].

temperature range are typical of an intermediate valent state for cerium as it is shown for the two allotropic varieties of $CeIr_2Si_2$.[65] From the ionic two-level (I.C.F.) proposed by Sales and Wohlleben, using a pseudo-Boltunann statistics[72] the average valence of cerium has been deduced and its thermal variation is shown in the inset of Figure 27.
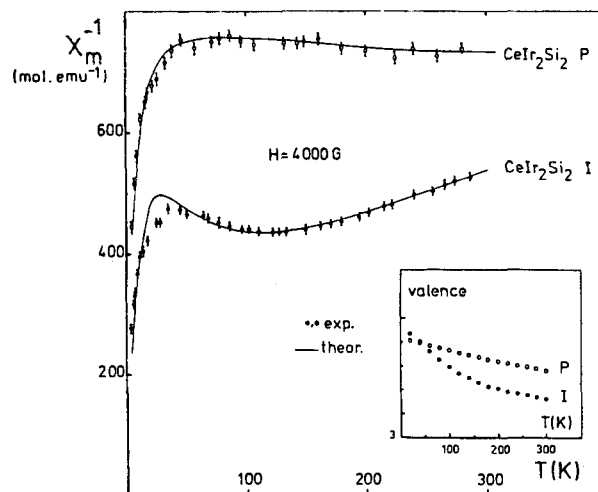
Figure 27. Experimental and calculated reciprocal susceptibilities vs temperature for the two modifications of $CeIr_2Si_2$ (Inset: thermal variation of the valence state of cerium).
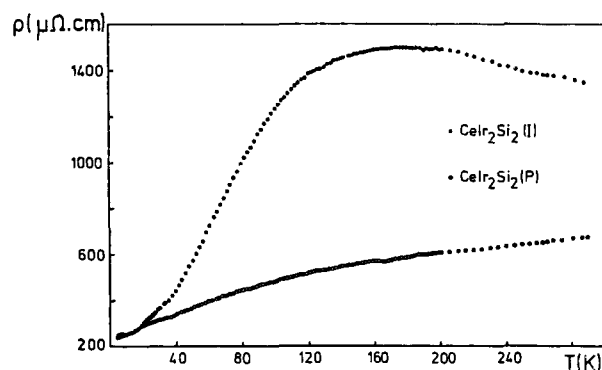
Figure 28. Thermal variation of the electrical resistivities of the (P) and (I) varieties of $CeIr_2Si_2$.

Conculusion

The main goal of this paper was to show the power of the X-ray absorption spectroscopy (XANES and EXAFS) for characterizing both crystalline and amorphous solids from structural (local order) and electronic point of view. After recalling the main principles of the XAS spectroscopy and mentioning the last developments dealing with multiple scattering phenomenon, some non-trivial examples have been chosen for showing that XAS spectroscopy is in certain cases, the only technique for bringing a definitive answer as for example: the local structural distortion of Li_{1-z}-$Ni_{1+z}O_2$ and the characterization of copper pairs in $CuZr_2$-$(PO_4)_3$ phosphate. In the other cases reported in this paper, XAS spectroscopy was decisive in combination with other characterization methods (X-ray and neutron diffraction experiments, Raman, EPR and Mössbauer spectroscopies, magnetic measurements, *etc.*) for characterizing local ordering and electronic structures of solids. The examples reported in this paper are rather taken in the field of solid state chemistry. However XAS spectroscopy is also a relevant technique for characterizing organometallic and molecular materials. In order to illustrate this last point let us mention briefly two interesting examples (i) the characterization of chemical bonds in bimetallic cyanides which are high T_c molecular based magnets; from L_{23} edges X-ray absorption and comparison with ligand field multiplet theory some parameters have been detennined as: crystal field parameters 10 Dq, spin-orbit coupling constants on the 2p and 3d shells, the degree of delocalization of the 3d electrons, the amount of charge transfer and its nature[73] (ii) the iron-(II) and iron (III) basket-handle porphyrins, which belong to a family of compounds designed in order to mimic the microenvironment of the active sites and the characteristics of the metallic centre, the stereochemistry and the coordination number, the oxidation and spin states; all these parameters are closely related to the biological function of haemoproteins: for example from XANES and EXAFS studies it has been shown that synthetic hemoprotein analogues, the dioxygen adduct 3 may be better formulated as $Fe^{II}(O_2)$ than by $Fe^{III}(O_2^-)$ which was proposed for the biological oxyhaemoglobin and oxymyoglobin analogues and furthermore the XANES spectra were sufficiently different for being used as a local structural probe for following the oxidation kinetics of an iron (II) to hydroxoiron (III) basket handle porphyrin.[74]

It is worthwhile noting that all the studies reported in this paper has been made thanks to the use of the synchrotron radiation source which offers more and more new opportunities due to the X-rays photon beams which are weakly divergent, highly brilliant, polarized and pulsed. Due to the outstanding features of the X-rays synchrotron radiation many special devices dealing with the structural characterization of solids have been recently developed as for example (i) the in situ Quick EXAFS-X-ray diffraction combination used on the same specimen of catalyst during the conversion of reactants into products;[75-78] an illustrative case is that of the catalyst $CuO/ZnO/Al_2O_3$ used in the methanol synthesis[79] (ii) the EXAFS spectroscopy used at very high temperature (up to 2700 K) for examining molten samples in order to study the local ordering in iiquids and the liquid →solid transition[80] (iii) the EXAFS spectroscopy for following *in situ* phase transitions under high pressure (*e.g.* CaN;[81] H_2O solid[82]].

References

1. *Synchrotron Radiation Research*; Winick, H.; Doniach, S., Eds.; Plenum Press: New York, 1980.
2. *EXAFS Spectroscopy: Techniques and Applications*; Teo, B. K.; Joy, D. C., Eds.; Plenum Press: New York, 1980.
3. *X-ray Absorption: Principle, Applications, Techniques of EXAFS, SEXAFS and XANES*; Koningsberger, D. C.; Prins, R., Ed.; Wiley: New York, 1988.
4. *EXAFS and Near Edge Structure*; Bianconi, A.; Incoccia, L.; Stiprich, Eds.; Springer Series in Chemical Physics, Springer-Verlag: Berlin, 1983; Vol. 27.
5. Sayers, D. E.; Stern, E. A.; Lytle, F. W. *Phys. Rev. Lett.* **1971**, *27*, 1024.
6. Greaves, G. N.; Dent, A. J.; Dobson, B. R.; Kalbitzer, S.; Pizzini, S.; Muller, G. *Phys. Rev.* **1992**, *B45*, 6517.
7. Teo, B. K.; Lee, P. A.; Simons, A. L.; Eisenberg, P.; Kindkai, B. M. *J. Am. Chem. Soc.* **1977**, *99*, 3854.
8. Petrau, J.; Calas, G.; Sainctavit, P. In *Proceedings of the International Conference on X-ray and Inner-shell Process*; Paris, France, 1987 [*J. Phys. Paris Colloq. 48*, C9-1085, 1987].
9. Kuzmin, A.; Purans, J. *J. Phys. Condens. Matt.* **1993**, *5*, 9423.
10. Kuzmin, A.; Purans, J.; Benfatto, M.; Natoli, C. R. *Phys. Rev.* **1993**, *B47*, 2480.
11. Kuzmin A.; Grisenti, R. *Phil Mag.* **1994**, *B70*, 1161.
12. Prouzet, E. *J. Phys. Condens. Matt.* **1995**, *2*, 8027.
13. Rehr, J. J.; Albers, R. C.; Zabinski, S. I. *Phys. Rev. Lett.* **1992**, *69*, 3397.
14. Rehr, J. J. *Jpn. J. Appl. Phys.* **1993**, *32*, 8.
15. Thomas, M. G. S. R.; David, W. I. F.; Goodenough, J. B. *Mat. Res. Bull.* **1985**, *20*, 1137.
16. Broussely, M.; Perton, F.; Labat, J.; Staniewiez, R. J.; Romero, A. *J. Power Sources* **1993**, *43/44*, 209.
17. Ohzuku, T.; Iwakoshi, Y.; Sawai, K. *J. Electrochem. Soc.* **1993**, *140*, 1751.
18. Broussely, M.; Perton, F.; Biensan, Ph.; Bodet, J. M.; Labat, J.; Lecerf, A.; Delmas, C.; Rougier, A.; Peres, J. P. *J. Power Sources* **1995**, *54*, 109.
19. Morales, J.; Peres-Vicente, C.; Tirado, J. L. *Mat. Res. Bull.* **1990**, *25*, 623.
20. Rougier, A.; Gravereau, P.; Delmas, C. *J. Electrochem. Soc.* **1996**, *143*, 1168.
21. Goodenough, J. B.; Wickham, D. G.; Croft, W. J. *J. Phys. Chem. Solids* **1958**, *5*, 107.
22. Li, W.; Reimers, J. N.; Dahn, J. R. *Solid State Ionics* **1993**, *62*, 123.
23. Peres, J. P.; Delmas, C.; Rougier, A.; Broussely, M.;

Perton, F.; Biensan, P.; Willmann, W. *J. Phys. Chem. Solids* **1996**, *57*, 1057.

24. Rougier, A. These Universite Bordeaux 1, N° 1644, 1996.

25. Rougier, A.; Delmas, C.; Chadwick, A. V. *Solid State Comm.* **1995**, *94*, 123.

26. Peres, J. P. These Universite Bordeaux 1, N° 1296, 1996.

27. Peres, J. P.; Demourgues, A.; Delmas, C. *Solid State Ionics* (to be published).

28. Rougier, A.; Saadoune, I.; Gravereau, P.; Willmann, P.; Delmas, C. *Solid State Ionics* **1996**, *90*, 83.

29. Takeda, Y.; Imanishi, N.; Nakahara, K.; Yamamoto, O.; Takano, M. (private communication).

30. Reimers, J. N.; Rossen, F.; Jones, C. D.; Dahn, J. R. *Solid State Ionics* **1993**, *61*, 335.

31. Bush, T. S.; Richard, C.; Catlow, A.; Chadwick, A. V.; Cole, M.; Geatches, R. M.; Greaves, G. N.; Tomlison, S. M. *J. Mat. Chem.* **1992**, *2*, 309.

32. Lines, M. E.; Glass, A. M. *Principles and Applications of Ferroelectrics and Related Materials*; Clarendon Press: Oxford, 1977.

33. Rauber, A. In *Current Topics in Materials Science*; Kaldis, E., Ed.; North Holland: Amsterdam, **1978**, *1*, 1.

34. Pepper, D. M. *Opt. Eng.* **1982**, *21*, 156.

35. Gunter, P. *Phys. Rep.* **1982**, *93*, 199.

36. Keune, W.; Date, S. K.; Gonser, U.; Bunzel, H. *Ferroelectrics* **1976**, *13*, 443.

37. Schirmer, O. F.; Thiemann, O.; Wöhlecke, M. *J. Phys. Chem. Solids* **1991**, *3*, 4135.

38. Serghini, A.; Kacimi, M.; Zyiad, M.; Brochu, R. *J. Chem. Phys., Phys. -Chim. Biol.* **1988**, *85*, 499.

39. Le Polles, G.; Parent, C.; Olazcuaga, R.; Le Flem, G.; Hagenmuller, P. *C. R. Acad. Sc. Ser. II* **1988**, *306*, 765.

40. Boutinaud, P.; Parent, C.; Le Flem, G.; Pedrini, C.; Moine, B. *J. Phys. Condens. Matter* **1992**, *4*, 3031.

41. Bussereau, I.; Belkhira, M. S.; Gravereau, P.; Boireau, A.; Soubeyroux, J. L.; Olazcuaga, R.; Le Flem, G. *Acta Cryst.* **1992**, *C48*, 1741.

42. Rath, N. P.; Holt, E.; Tanimura, K. *Inorg. Chem.* **1985**, *24*, 3934.

43. Mehotra, P. K.; Hoffmann, R. *Inorg. Chem.* **1978**, *17*, 2187.

44. Boutinaud, P.; Garcia, A.; Parent, C.; Faucher, M.; Le Flem, G. *J. Phys Chem. Solids* **1995**, *9*, 1147.

45. Fargin, E.; Bussereau, I.; Le Flem, G.; Olazcuaga, R.; Cartier, C.; Dexpert, H. *Eur. J. Solid State Inorg. Chem.* **1992**, *29*, 975.

46. Fargin, E.; Bussereau, I.; Olazcuaga, R.; Le Flem, G.; Cartier, C.; Dexpert, H. *J. Solid State Chem.* **1994**, *112*, 176.

47. McCarron, E. M.; Calabrese, J. C.; Subramanian, M. B. *Mat. Res. Bull.* **1987**, *22*, 1421.

48. Parent, C.; Boutinaud, P.; Le Flem, G.; Moine, B.; Pedrini, C.; Garcia, D.; Faucher, M. *Optical Materials* **1994**, *4*, 107.

49. Greaves, G. N. *Glass Science and Technology* **1990**, *48*, 1.

50. Gurman, S. J. In *Application of Synchrotron Radiation*; Catlow, C. R. A.; Greaves, G. N., Eds.; Blackie: Glasgow, 1990; p 140.

51. Vogel, E. M.; Weber, M. J.; Krol, D. M. *Phys. Chem. Glasses* **1991**, *32*, 231.

52. Lines, M. E. *Phys. Rev.* **1991**, *B43*, 11478.

53. Cardinal, T.; Fargin, E.; Flem, G. LE.; Couzi, M. *J. Solid State Chem.* **1995**, *120*, 151.

54. Cardinal, T.; Fargin, E.; Le Luyer, Y.; Le Flem, G.; Canioni, L.; Segonds, P.; Sarger, L.; Adamietz, F.; Ducasse, A. *Nucl. Intr. and Meth. In Phys. Res.* **1995**, *B97*, 169.

55. Kugel, G. E.; Brehat, F.; Wyncke, B.; Fontana, M. D.; Marnier, G.; Caratabos-Nedelec, C.; Mangin, J. *J. Phys. C: Solid State Phys.* **1988**, *21*, 5565.

56. Bailar, J. C.; Hemeleus, H. J.; Nyholm, R.; Wong, J.; Trotman-Dickenson, A. F. In *Comprehensive Inorganic Chemistry*; Bailar, J. C. et al. Eds.; Pergamon: Oxford, **1973**, *3*, 317.

57. Blasse, G.; Van Den Hvevel, G. P. M. *J. Solid State Chem.* **1974**, *10*, 206.

58. Bertoluzza, A.; Marinangelli, A.; Morelli, M. A.; Simon, R. *J. Non-Cryst. Solids* **1981**, *45*, 149.

59. Cardinal, T.; Fargin, E.; Le Flem, G.; Canioni, L.; Segonds, P.; Sarger, L.; Adamietz, F.; Ducasse, A. *Eur. J. Solid State J-norg. Chem.* **1994**, *31*, 935.

60. Berthereau, A.; Fargin, E.; Villesuzanne, A.; Olazcuaga, R.; Le Flem, G.; Ducasse, L. *J Solid State Chem.* **1996**, *126*, 143.

61. Nasu, H.; Uchigaki, T.; Nakamura, M.; Kamiya, K. *Proceedings, International Conference of Science and Technology of New Glasses*; Tokyo, 1991; p 175.

62. Nasu, H., Ibara, Y.; Kubodera, K. *J. Non-Cryst. Solids* **1989**, *110*, 229.

63. Berthereau, A.; Le Luyer, Y.; Olazcuaga, R.; Le Flem, G.; Couzi, M.; Canioni, L.; Segonds, P.; Sarger, L.; Ducasse, A. *Mat. Res. Bull.* **1994**, *29*, 933.

64. Sekiya, T.; Mochida, N.; Ohtsuka, A.; Tonokawa, M. *J. Non-Cryst.* **1994**, *168*, 106.

65. Buffat, B.; Chevalier, B.; Tuilier, M. H.; Lloret, B.; E-tourneau, J. *Solid State Comm.* **1986**, *59*, 17.

66. Wang-Xian-Zhong, Lloret, B.; Lam Ng, Wee.; Chevalier, B.; Etourneau, J.; Hagenmuller, P. *Rev. Chim. Min.* **1985**, *22*, 711.

67. Braun, H. F.; Engel, N.; Parthe, E. *Phys. Rev.* **1983**, *B28*, 1389.

68. Lejay, P.; Higashi, I.; Chevalier B.; Hirjak, M.; E-tourneau, J.; Hagenmuller, P. *Acad. Sc.* **1983**, *236*, 1583.

69. Hirjak, M.; Chevalier, B.; Etourneau, J.; Hagenmller, P. *Mat. Res. Bull.* **1984**, *19*, 727.

70. Demourgues, A.; Chevalier, B.; Fourgeot, F.; Darriet, J.; Etourneau, J. *Nuclear Instruments and Methods in Physics Res.* **1995**, *B97*, 460.

71. Herbst, J. F.; Wilkins, J. W. *Phys. Rev.* **1982**, *B26*, 1689.

72. Sales, B. C.; Wohlleben, D. K. *Phys. Rev. Lett.* **1975**, *35*, 1240.

73. Arrio, M. A.; Sainctavit, Ph.; Cartier, C.; Moulin, dit.; Mallah, T.; Verdaguer, M.; Pellegrin, E.; Chen, C. T. *J. Am. Chem. Soc.* **1996**, *118*, 6422.

74. Cartier, C.; Moulin, dit.; Momenteau, M.; Dartyge, E.; Fontane, A.; Tourillon, G.; Michalowicz, A.; Verdaguer, M. *J. Chem. Soc., Dalton Trans.* **1992**, 609.

75. Clausen, B. S.; Graback, K.; Steffensen, G.; Hansen, P.

X-Ray Absorption Spectroscopy

Bull. Korean Chem. Soc. **1998**, Vol. 19, No. 1 21

L.; Topsoe, H. *Catal. Lett.* **1993**, *20*, 23.

76. Als Nielsen, J.; Grubel, G.; Clausen, B. S. *Proceedings 1st European Conf. on Synchrotron Radiation in Materials Science*; Chester, UK, 1994. *Nucl. Instr. and Meth.* **1995**, *B97*, 522.

77. Thomas, J. M.; Greaves, G. N.; Catlow, C. R. A. *Nucl. Instr. And Math.* **1995**, *B97*. 1.

78. Thomas, J. M.; Greaves, G. N. *Catal. Lett.* **1993**, *20*, 337.

79. Clausen, B. S.; Grabaer, L.; Steffensen, G.; Hansen, P.

L.; Topsoe, H. *Catal. Lett.* **1993**, *20*, 23.

80. Landron, C.; Launay, X.; Riffet, J. C.; Etchegut, P.; Auger, Y.; Ruffier, D.; Coutures, J. P.; Lemonier, M.; Gailhanou, M.; Bessiere, M.; Bazin, M.; Dexpert, H. *Nucl. Intr. And Meth.* **1997**, *B124*, 627.

81. Itie, J. P.; Polian, A.; Calas, A.; Petiau, J.; Fontaine, A.; Tolentino, H. *Phys. Rev. Lett.* **1989**, *63(4)*, 398.

82. Loubeyre, P.; Le Toullec, R.; Haneland, M.; Hausermann, D. (to be published).